# Chapter 7

# Synthesis and Characterisation of $SnO_2$/ Graphene Nano-Composite

## 7.1 Introduction

Metamaterials are artificially structured materials designed to exhibit electromagnetic properties not commonly found in naturally occurring substances[9–11]. Among these properties, negative permittivity and negative permeability have been of particular interest, as they enable unique wave propagation phenomena such as negative refraction, reverse Doppler effects[14,214], and backward Cherenkov radiation. According to existing theory, $\varepsilon<0$ arises when the free-carrier plasma frequency $\omega_p$ exceeds the operating frequency[8]. While metals inherently satisfy this condition, their high charge carrier densities push $\omega_p$ into the infrared or optical range.

Metamaterials are generally classified into two main categories: periodic and disordered (random) structures. Periodic metamaterials typically involve arrays of metallic elements—such as wires or split-ring resonators—engineered to interact with electromagnetic waves through resonant coupling mechanisms. These structures have been successful in achieving both negative permittivity and permeability at specific frequency ranges. However, they present several limitations in terms of fabrication complexity, cost, and limited flexibility in tuning, and the tendency to exhibit overly high negative permittivity values, which are often unsuitable for devices requiring controlled dielectric behavior.

To address the challenges associated with periodic structures, recent research has focused on disordered composite metamaterials, which consist of a conductive phase dispersed within an insulating matrix. These systems allow for greater design flexibility and easier fabrication, as their electromagnetic response can be tuned by adjusting parameters such as filler concentration, particle morphology, and spatial distribution. Conductive Metal Composites

(CMCs) and Polymer Matrix Composites (PMCs), which incorporate metallic fillers like silver, copper, nickel, and iron, have traditionally been employed to achieve negative permittivity[5]. While effective, these metals present several well-known drawbacks: high density, proneness to oxidation, limited mechanical flexibility, and difficulty in precisely controlling both conductivity and permittivity. These limitations hinder their broader applicability, especially in systems where moderate dielectric behavior, lightweight design, or chemical stability are critical.

While ENG materials are advantageous for attenuating EM wave like in EMI shielding and ideal for applications like Faraday cage, their high conductivity also leads to significant surface reflection, which is undesirable for stealth applications, where minimal reflection and maximal absorption are critical[131]. Achieving perfect electromagnetic absorption requires a balance between minimizing surface reflection (via impedance matching with free space) and maximizing energy dissipation within the material[168,215,216]. This condition is met in the epsilon-near-zero (ENZ) condition, where the real part of the complex permittivity ($\varepsilon = \varepsilon' + i\varepsilon''$) approaches zero, and the imaginary part remains finite. In this regime, the material's impedance ($z = \sqrt{(\mu_r/\epsilon_r)}$ ) approaches that of free space ($Z_0$ = 377 ohm), minimizing reflection. Simultaneously, finite losses ($\epsilon''$) ensure significant attenuation of the transmitted wave, resulting in nearly perfect absorption[217,218].

To mitigate these issues, there is growing interest in using materials that offer ***moderate electrical conductivity*** while still supporting negative permittivity, particularly in the radio frequency (RF) domain, where many practical electromagnetic devices operate.

However, a key challenge remains: the minimum conductivity threshold required to sustain ENG behavior in disordered systems is still not fully understood, particularly for non-metallic fillers. This uncertainty makes it essential to explore alternative materials that can meet both structural and functional requirements.

In this study, we intentionally selected graphene as the conductive phase in graphene/$SnO_2$ composites for two key reasons.[107,219–221] First, due to its high surface-to-volume ratio and two-dimensional structure, graphene enables the formation of conductive networks at significantly lower filler concentrations compared to conventional metallic fillers. This increases the likelihood of achieving negative permittivity at low loading levels, helping preserve the insulating matrix. Second, graphene offers excellent electrical conductivity while being lightweight, making it a practical alternative to metals for applications where minimizing material weight is essential.

The study focuses on two main objectives: (i) to systematically study how electrical conductivity evolves with increasing graphene content and to determine the threshold conductivity required to induce epsilon-negative (ENG) behavior, and (ii) to achieve epsilon-near-zero (ENZ) characteristics by carefully adjusting not just the filler concentration but also external parameters such as temperature. $SnO_2$ was chosen as the insulating matrix for its good chemical and thermal stability, electrical insulation, and compatibility with carbon-based fillers. The composites were prepared using a wet mechanical mixing process to ensure uniform dispersion of graphene within the matrix.

We investigated the dielectric behavior of two $SnO_2$ /graphene composites—SGR2 (98 wt% $SnO_2$ / 2 wt% graphene) and SGR4 (96 wt% $SnO_2$ / 4 wt% graphene)—across a range of

frequencies and temperatures. In SGR2, where the graphene content remains below the percolation threshold, the permittivity is largely positive and near zero at room temperature but transitions to negative values with increasing temperature. This behavior was modeled using the Debye formalism below the conductivity threshold, while the Drude-Lorentz model was applied above it to better capture free-carrier contributions and to determine the threshold conductivity required for negative permittivity. These results were further validated by previously reported data.

Above the percolation threshold, as in SGR4, the permittivity becomes strongly negative and the composite exhibits metallic-like conductivity. Composites demonstrating epsilon-near-zero (ENZ) characteristics primarily dissipate electromagnetic energy via absorption, making them effective for stealth and absorbing-layer applications. In contrast, highly conductive composites with large negative permittivity tend to reflect incident waves due to impedance mismatch. This dual behavior underscores the tunability of $SnO_2$/graphene systems and their suitability for EMI shielding applications, where selective absorption or reflection is desired based on operational frequency and filler concentration. This study pave pathway toward multifunctional, next-generation electromagnetic materials for applications in EMI control, radar absorption, and adaptive metamaterials.

## 7.2 Sample Preparation

To synthesize the $SnO_2$–graphene nanocomposites, **wet chemical method** was employed to ensure homogeneous dispersion and interfacial interaction between the two components. Initially, **commercial $SnO_2$ powder** was subjected to **planetary ball milling** at **120 rpm for 24 hours** using **acetone** as the mixing medium to avoid oxidation, minimize agglomeration

during composite formulation and to aid in uniform particle dispersion to reduce particle size and improve compatibility with the commercial graphene nanoplatelets (GNPs), which inherently possess a much smaller lateral dimension. The resulting slurry was subsequently **dried in a conventional oven at 60 °C for 24 hours** to evaporate residual solvent and recover the fine $SnO_2$ powder.

Following this, **composites were formulated by mixing $SnO_2$ with graphene nanoplatelets** in two stoichiometric ratios:

- **SGR2**: 98 wt.% $SnO_2$ + 2 wt.% graphene
- **SGR4**: 96 wt.% $SnO_2$ + 4 wt.% graphene

The powders were manually mixing using an **agate mortar and pestle for 6 hours** to ensure better homogeneity. **Ball milling was intentionally avoided during this step**, as excessive mechanical energy can generate localized heat due to friction between the balls and the milling jar. Such uncontrolled thermal effects can damage the delicate two-dimensional morphology of graphene, potentially degrading its structural integrity and thereby altering its electrical and dielectric properties in the final composite.

After achieving a uniform powder mixture, **2 wt.% polyvinyl alcohol (PVA)** was added as a temporary binder to aid pellet formation. **Cylindrical pellets** of **10 mm diameter and 2 mm thickness** were pressed using a uniaxial hydraulic press. The pellets were subsequently **dried at 250 °C** to remove the PVA and enhance the mechanical integrity and compactness of the final samples. The detailed steps involved in sample preparation is shown in Figure **7.1**.

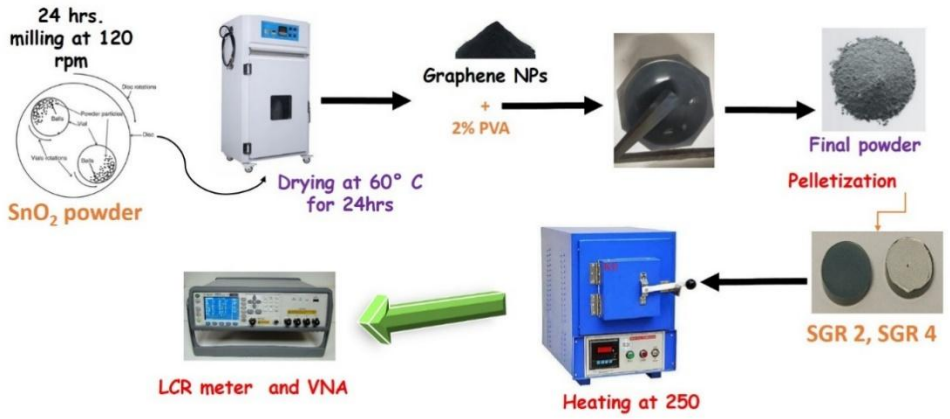


***Figure 7.1 The step-by-step process of synthesis the SGR composites.***

Pellets were characterized by X-ray diffraction (XRD) to confirm phase purity and crystallographic structure. Surface morphology and grain connectivity were examined using scanning electron microscopy (SEM). The complex permittivity and electrical conductivity were investigated over the frequency range of 20 Hz to 1 MHz using an LCR meter, with measurements conducted from room temperature up to 250 °C. For **microwave property measurements**, the sintered pellets were **crushed into fine powder** and mixed with **20 wt.% epoxy resin (powder: epoxy- 4:1)** to form a homogeneous composite suitable for waveguide-based analysis. The epoxy-composite mixture was molded and cured inside a **WR-90 rectangular waveguide sample holder**, optimized for measurements in the X-band frequency range.

## 7.3 Characterization Techniques

Structural characterization of the prepared composites was carried out using **X-ray diffractometer** (Rigaku X'PERT PRO MPD**)** with Cu Kα radiation (λ = 1.5406 Å) to verify phase purity and assess potential lattice distortions upon graphene incorporation. **Field emission scanning electron microscopy (FESEM)** (SEM, ZEISS, USA) was used to examine

particle morphology, grain connectivity, and dispersion uniformity within the composite matrix. **Dielectric and electrical measurements** in the Radio-frequency range (20 Hz to 1 MHz; temperature range from RT – **250 °C)** were performed using a **Keysight E4980A precision LCR meter** in a parallel-plate configuration. Conductive Silver paste was applied to both pellet faces to ensure good electrical contact. The real (ε′) and imaginary (ε″) components of the complex permittivity were extracted as a function of frequency to probe dipolar and interfacial polarization mechanisms. Microwave characterization was carried out using standard WR-90 rectangular waveguide holders, with scattering parameters ($S_{11}$, $S_{21}$) measured in the X-band (8.2–12.4 GHz) using a Keysight PNA N5230C vector network analyser.

## 7.4 Results and Discussion

The structural analysis of the synthesized $SnO_2$–graphene nanocomposites was performed using X-ray diffraction (XRD), as shown in Figure **7.2.** To confirm the structural integrity and purity of the graphene nanoplatelets (GNPs), the XRD pattern of pristine graphene is included in the Figure7.2 (a). The spectrum reveals a broad (002) reflection peak near **2θ ≈ 26°**, along with a minor peak near **35°**, typically associated with partially oxidized or few-layer graphene[222]. In Figure **7.2 (b)**, both **SGR2** and **SGR4** compositions, the diffraction patterns are dominated by the characteristic peaks of tetragonal $SnO_2$ (cassiterite phase), indicating that the primary crystalline phase remains mostly unchanged upon graphene incorporation[191]. The absence of prominent diffraction peaks corresponding to graphene is expected, given its low filler content (2–4 wt.%), which falls below the detection limit of conventional XRD due to the weak scattering cross-section and amorphous nature of few-layer graphene. All observed peaks in the composite samples were indexed to standard $SnO_2$ reflections using reference CIF files and verified via peak-matching analysis using "**MATCH" software**. The absence of

secondary phases and lack of any significant peak shifts suggest that the graphene does not substitute into the $SnO_2$ lattice, nor does it induce strain or distortion within the host matrix. This implies that the composite retains a **two-phase structure**, with graphene remaining physically dispersed rather than chemically integrated within the $SnO_2$ crystal lattice.

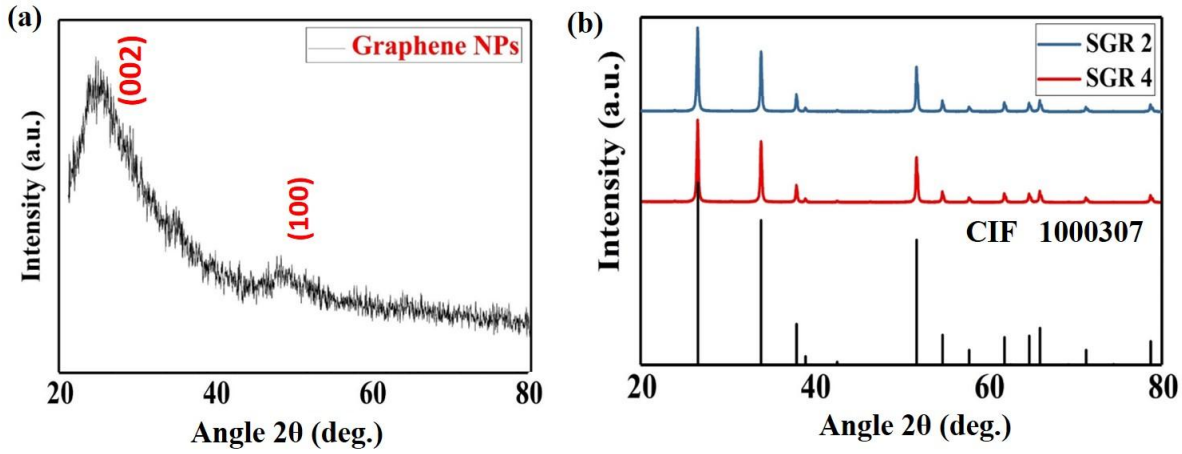


***Figure 7.2 The XRD pattern of (a) pure graphene (b) the SGR (2, 4%) composites. XRD peaks in SGR composites dominated by the $SnO_2$ as confirm by the reference CIF of $SnO_2$.***

## 7.5 Electrical Properties

The dielectric behavior of the SGR composites was investigated over a frequency range of 20 Hz to 1 MHz and temperatures ranging from room temperature to 250 °C. The real part of the permittivity (ε′) for the SGR2 sample is presented in Figure 7.3. At room temperature, ε′ remains positive and nearly constant across the entire frequency spectrum, indicating a dielectric-dominated response with an insufficient free carrier concentration to induce metallic or plasmonic characteristics. This response, characterized by an epsilon-near-zero (ENZ) feature, suggests that the system is close to the percolation threshold but has not yet attained the critical carrier density required to drive ε′ into negative values[223–225].

With increasing temperature, thermal excitation enhances carrier mobility and/or density, resulting in a gradual decrease in ε′. Around 150 °C, ε′ approaches zero, indicating the onset of ENZ behavior under thermally activated conditions. Beyond this temperature, ε′ crosses into the negative regime and becomes increasingly negative with further temperature elevation, signifying a transition toward a plasmonic or metallic-like dielectric response.

At temperatures below **150 °C**, and frequencies below 500 Hz, space-charge polarization commonly referred to as Maxwell–Wagner polarization is dominated[51,196,226]. This effect occurs at the interfaces between the silver-coated surfaces and the metallic sample holders, as well as between the conductive graphene nanoplatelets and the insulating $SnO_2$ particles. The difference in conductivity between these components leads to the accumulation of charge at the interfaces, generating a local electric field that contributes to the overall polarization response of the composite. The charge carriers have sufficient time to accumulate at these interfaces before the applied electric field reverses direction, leading to a relatively high permittivity due to the substantial charge buildup at the conductive-insulating interfaces.

In Figure 7.3 (a), the observed plateau region between 100 Hz and 1 MHz corresponds to a transitional frequency window, where the space-charge effects are largely suppressed due to the field reversals occur too rapidly for charge accumulation, and their ability to redistribute at the interfaces weakens, leading to a decrease in permittivity. The permittivity exhibits minimal frequency dependence, suggesting that the system has reached a dynamic equilibrium,and the dielectric response is now govern by intrinsic mechanisms, such as dipolar or orientational polarization, arising from the reorientation of bound charges within the insulating matrix and at localized defect sites[227–229].

Temperature after 150 °C, thermal excitation plays a critical role in the nature of the permittivity by modifying the electronic occupation, particularly near the Fermi level[230]. $SnO_2$, a wide-bandgap semiconductor (~3.6 eV), contains donor-like shallow states near the conduction band edge due to intrinsic oxygen vacancies[194]. At room temperature, these states are only partially ionized. As the temperature increases, thermal excitation supplies sufficient energy for electrons in these shallow traps to ionize and transition into the conduction band, leading to an increase in free carrier density, n(T). This ionization process follows Fermi–Dirac statistics, where the occupation of the conduction band is determined by the balance between thermal excitation and the available state.

$$n\,(T) = N_c \exp(-\frac{E_c - E_F}{k_B T}) \qquad (7.1)$$

Where, $Nc$ is the effective density of states in the conduction band, $E_c - E_F$ is the activation energy, and $k_B$ the Boltzmann constant. Once $n(T)$ exceeds a critical value, the collective motion of delocalized electron begins to dominate the dielectric response.

At temperatures above 150 °C, the real part of the permittivity (ε′), which at lower temperatures is governed primarily by interfacial (Maxwell–Wagner), dipolar, and orientational polarization mechanisms, begins to exhibit negative values. This indicates that the response is increasingly dominated by displacement currents associated with thermally activated free carriers oscillating out of phase with the applied electric field, a characteristic feature of the Drude-type response[36].

However, from Figure 7.3 (b) and (c) analysis of the permittivity spectra beyond this temperature range reveals deviations from a purely Drude-like behavior. Specifically, the

presence of two broad dispersive features in the ε′(f) plot suggests the contribution of additional relaxation mechanisms. These features are not consistent with only plasma oscillation model proposed by Drude and imply the presence of bound charge oscillations superimposed on the free-carrier response.

To quantitatively examine this, we initially fit the experimental data with standard Drude model[231].

According to the Drude's model, relative permittivity is given as:

$$\varepsilon_r' = 1 - \frac{\omega_p^2}{\omega_\tau^2 + \omega^2} \qquad (7.2)$$

$$where\ \omega_p = \sqrt{\frac{n_{eff}.e^2}{m^{*2}.\varepsilon_0}} \qquad (7.3)$$

Where $\omega_\tau$ is the damping frequency which is related to the relaxation time (τ) by the relation $\omega_\tau = 1/\tau$. It represents the characteristic frequency at which charge carriers lose momentum due to collisions, and $\omega_p$ is the Drude plasma frequency that is associated with the density of free carriers ($n_{eff}$), electronic charge ($e$), and effective mass ($m^*$).

The standard Drude model, which accounts only for delocalized free-electron dynamics, fails to capture the spectral shape—particularly in the regions where non-monotonic variations in ε′ are observed. In contrast, the Drude–Lorentz model, which includes resonant oscillations of bound charges in addition to the free-carrier term, provides a significantly improved fit. This agreement supports the interpretation that the observed negative permittivity arises not solely

from the free-carrier plasma response, but from a combined effect involving both thermally activated carriers and localized dipolar resonances.

According to this model, the real part of the complex permittivity ($\varepsilon_r'$) is described as follows[93,232,233]:

$$\varepsilon_r' = \varepsilon_\infty - \frac{\omega_{pd}^2}{\omega^2 + \omega_d^2} + \frac{\omega_{pl}^2(\omega_0^2 - \omega^2)}{(\omega_0^2 - \omega^2)^2 + \omega^2\gamma^2} \qquad (7.4)$$

where, $\varepsilon_\infty$ is the permittivity extrapolated towards high frequency, $\omega_{pl}$ is the Lorentz angular plasma frequency, $\omega_d$ is the damping frequency, $\omega_0$ is the resonance frequency or damping force, $\gamma$ damping coefficient of oscillating dipoles, $\omega_{pd}$ is the Drude angular plasma frequency, which is related to free charge carrier concentration ($n_{free}$), effective mass of free charge carriers ($m_{free}^*$) and, e is a charge of an electron (= $1.6\times10^{-19}$ C)

$$\omega_{pd} = \sqrt{\frac{n_{free}.e^2}{m_{free}^*.\varepsilon_0}} \qquad (7.5)$$

similarly, the Lorentz angular plasma frequency, $\omega_{pl}$ is related to bound charge carrier concentration ($n_{bou}$), effective mass of oscillating dipoles ($m_{bou}^*$) and, charge of dipole (q).

$$\omega_{pl} = \sqrt{\frac{n_{bou}.q^2}{m_{bou}^*.\varepsilon_0}} \qquad (7.6)$$

Thus, the dielectric behavior above 150 °C reflects a thermally induced crossover to a hybrid response regime, where **free and bound charge contributions coexist**—leading to the emergence of negative ε′ through a mechanism distinct from classical metallic behavior.

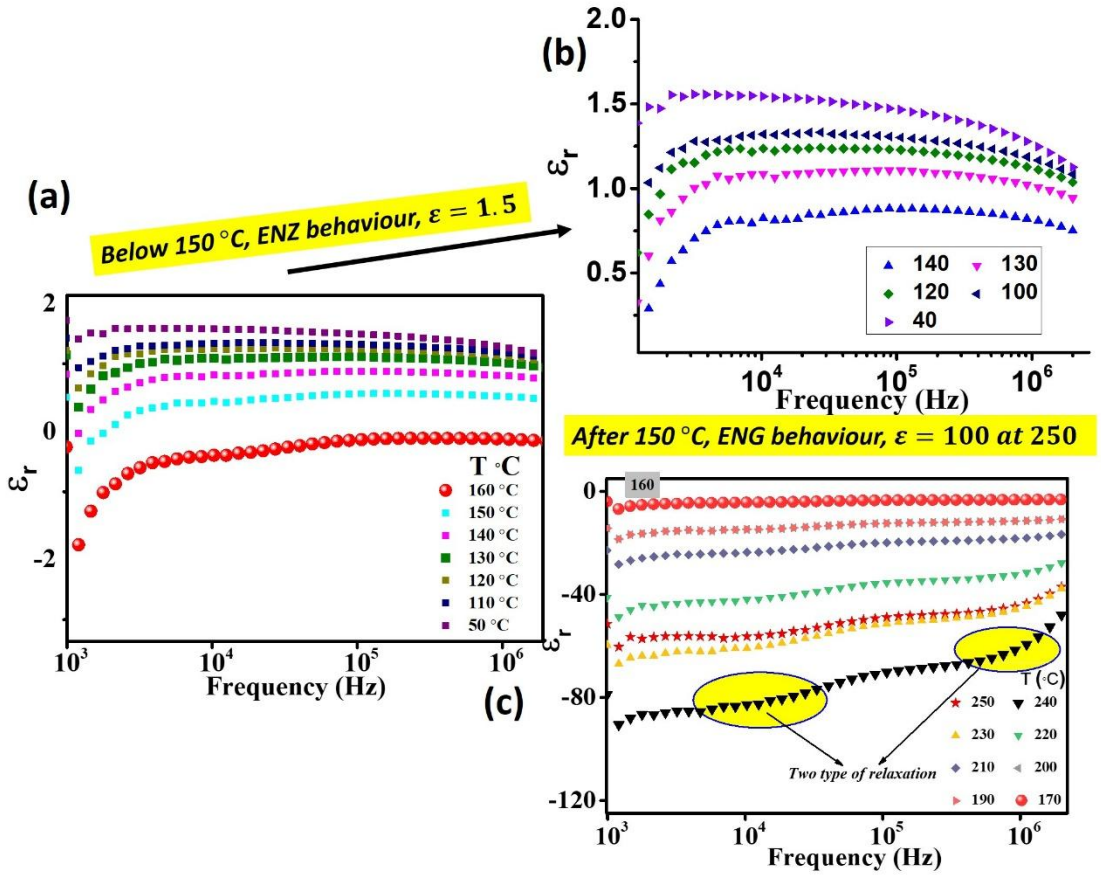


***Figure 7.3 The Frequency vs. Permittivity of SGR 2 composites is shown. (a) from room temperature to 160 below transition temperature (b) Zoomed version for a closer value (c) above transition temperature from 160 to 250.***

This behaviour can be further confirmed when the conductivity is replotted against the frequency at various temperature. The frequency-dependent behaviour of the **SGR2** composite provides insight into its underlying charge transport mechanisms. As shown in Figure 7.4 (a), the conductivity remains nearly constant across the low-frequency range (<$10^4$ Hz), indicative of a **DC-conductive regime** dominated by long-range carrier transport through thermally activated pathways. This frequency-independent plateau reflects the bulk conductivity of the system and is characteristic of materials exhibiting Ohmic behavior below the percolation threshold. At higher frequency (> $10^4$ Hz), and within the temperature range (< 150 °C) where

the real part of permittivity remains positive, the conductivity of SGR2 begins to rise gradually. This dispersive behavior follows conventional Jonscher's universal power law as shown in Figure 7.4 (c)[201,234].

The AC conductivity ($\sigma_{ac}$) is often described by the Jonscher′s Power Law (JPL) written as:

$$\sigma_{AC}(\omega, T) = A(\omega)^n \qquad (7.7)$$

Where, $A$ is a constant, $\omega$ $(= 2\pi f)$ is the angular frequency and $n$ is the frequency.

However, in Figure 7.4 (c), temperatures above ~150 °C further confirms that the, system transitions into the **negative permittivity region**, the high-frequency region of the conductivity plot begins to **decrease**, opposite from the earlier power-law trend observed in Figure 7.4 (b). This decline is attributed to the **skin effect**, wherein increased free carrier concentration leads to enhanced reflectivity and reduced electromagnetic field penetration[187,198]. Consequently, the current-carrying volume becomes confined to the near-surface region, leading to attenuation of the high-frequency response. This behavior is indicative of a shift toward **Drude-like conduction**, where delocalized charge carriers exhibit collective oscillations and finite relaxation times, resulting in a frequency-dependent suppression of AC conductivity.

According to this model, conductivity is related to various parameters as in the Eqn. (7.4):

$$\sigma_{ac} = \frac{\sigma_{dc}}{1 + \omega^2\tau^2} + \frac{\varepsilon_0 \omega_{pl}^2 \omega^2 \gamma}{(\omega_0^2 - \omega^2)^2 + \omega^2\gamma^2} \qquad (7.8)$$

where, $\sigma_{dc}$ is the dc limit of Drude conductivity, $\tau$ is the average scattering time of carriers, $\omega_{pl}$ is the Lorentz angular plasma frequency, $\omega_0$ is the resonance frequency, and $\gamma$ is the damping factor. The first part of Eqn. (7.8) represents the contribution of free electrons, while the second part to the resonance response of localized/bound electrons. In Figure 7.4 (b), symbols are experimentally measured data points and solid lines represent fitting according DL models. A good matching between measured data and data calculated according to Eqn. (7.8) is evidence of dominating role of the free charge carriers over bound charge carriers.

This transition—from Jonscher-type to Drude-type conductivity behavior—demonstrates the thermally driven evolution of SGR2 from a dielectric into a quasi-metallic regime. The observed response supports the conclusion that negative permittivity in this system is governed by an increase in free carrier density and the formation of an interconnected graphene network, which enables effective plasmonic behavior at relatively low temperatures.

To quantitatively determine the conductivity threshold at which the real part of permittivity ($\varepsilon'$) changes sign, we closely examined the temperature-dependent conductivity and permittivity data in the 100–180 °C range Figure 7.4 (d). At 150 °C, the composite exhibits a conductivity of ~0.2 S/m, while $\varepsilon'$ remains positive. As the temperature increases to 160 °C and 170 °C, the conductivity rises to ~0.4 S/m and ~0.6 S/m, respectively. It is at this point—around 0.6 S/m—that the sign reversal in $\varepsilon'$ is observed, indicating the onset of a negative permittivity regime. For further confirmation, we evaluated $\varepsilon'$ at 180 °C, where the conductivity remains above **0.3 S/m**, and the negative $\varepsilon'$ response is more pronounced and measurable.

These observations suggest that the critical threshold conductivity required to initiate a measurable, magnitutude of negative permittivity in this system is approximately **0.3 S/m**.

Previous theoretical reports have estimated a general threshold near **1 S/m** for negative ε′ to emerge. Our results refine this understanding by experimentally identifying a narrower window: ε′ approaches zero (ENZ regime) in the conductivity range of **0.2–0.5 S/m**, while the transition to clearly negative ε′ occurs above **0.5 S/m**. This provides a more precise basis for engineering tunable dielectric responses in oxide–graphene systems, enabling better control for device applications.

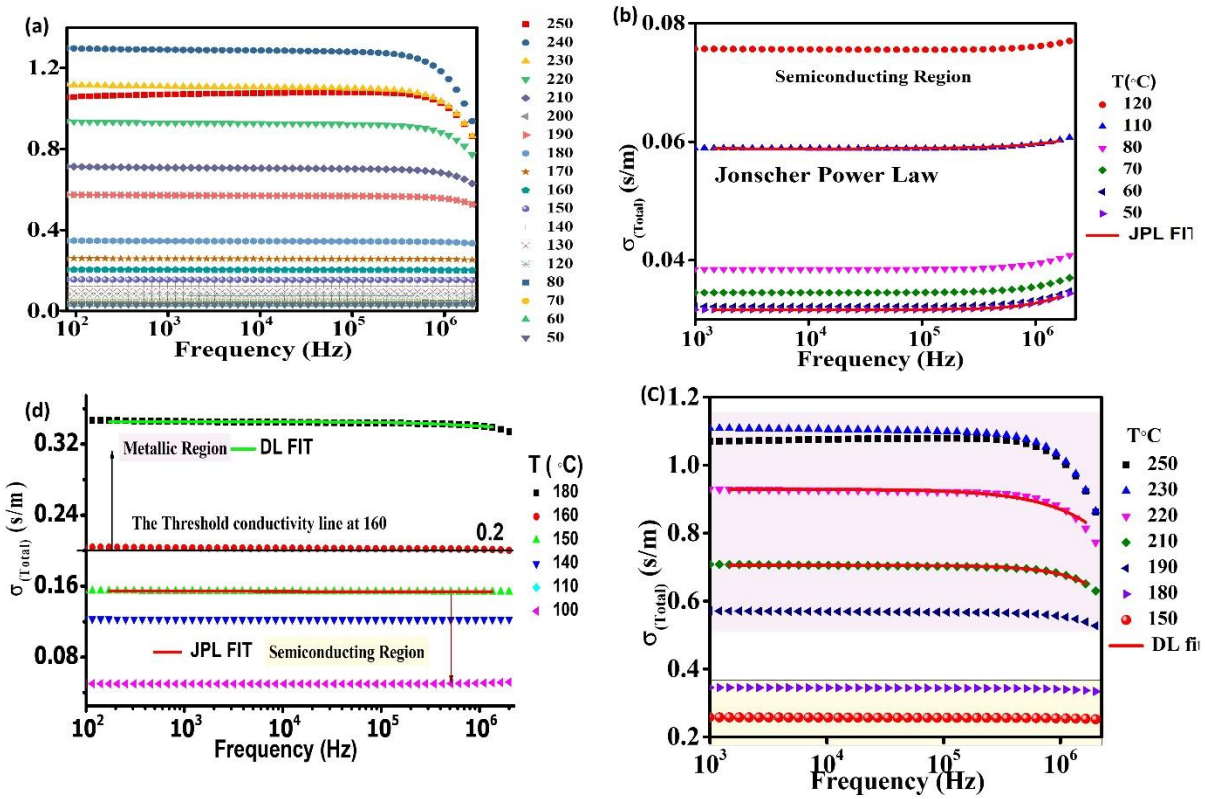


***Figure 7.4 The total conductivity of the SGR 2 composites (a) from room temperature to 250. (b) Below transition temperature with JPL fitting to verify the semiconducting nature below 160. (c) Total conductivity above the transition temperature, fitted by Drude model, (d) Comparison between the JPL fitted conductivity and Drude fitted conductivity to identified the threshold conductivity required for the generation of negative permittivity.***

The thermally induced transition from positive to negative permittivity previously has been observed in doped oxide semiconductors. For instance, Sn-doped $Sr_2MnO_4$ shows negative permittivity only at high temperatures (~600 °C).

To understand the correlation between permittivity and conductivity, and to determine the minimum conductivity required for the onset of negative permittivity, we examined two representative layered perovskite systems: $La_2NiO_4$[114] and Nb-doped $Sr_2MnO_4$[101]. Both materials are RP phase pervoskites, share a similar tetragonal crystal structure, and were studied under identical experimental conditions, with dielectric properties measured in the frequency range of 20 Hz to 2 MHz and temperatures from room temperature to 600 °C.

In Nb-doped $Sr_2MnO_4$, the permittivity displays a linear increase with conductivity as temperature rises, as evident from the plotted data. In contrast, $La_2NiO_4$ exhibits a nonlinear (polynomial) dependence, where permittivity and conductivity both increase with temperature but in a more complex relationship. Interestingly, beyond ~450 °C, $La_2NiO_4$ shows a simultaneous decline in both conductivity and permittivity, further reinforcing the observed correlation. These results confirm that although the exact relationship is material-specific, a consistent trend emerges; permittivity (including its sign and magnitude) is directly influenced by changes in conductivity.

A more detailed analysis of Sn-doped $Sr_2MnO_4$ reveals that negative permittivity can also be thermally activated[35]. Three compositions—SMS0, SMS3, and SMS5—were investigated for their temperature-dependent permittivity behavior. All samples exhibited a transition from positive to negative permittivity as temperature increased. In the undoped composition SMS0, negative permittivity emerged around 580–600 °C. With doping, this transition occurred at

significantly lower temperatures: approximately 360 °C for SMS5 and 300 °C for SMS3, indicating that doping facilitates earlier onset of epsilon-negative (ENG) behavior.

To understand this transition, the corresponding conductivity values near these temperatures were analyzed. Although direct measurements at the exact transition points were limited, interpolation from adjacent data points suggests that the conductivity lies between 0.1 and 0.5 S/m during the transition. This point indicates a transition from dipolar to plasma-like dielectric behavior, consistent with Drude conduction. A detailed examination of the real part of the permittivity, ε′(f), for the SMS0, SMS3, and SMS5 samples reveals a small hump superimposed on the main dispersion curve in the intermediate frequency range. At temperatures below the transition point, the permittivity is primarily governed by interfacial (Maxwell–Wagner), dipolar, and orientational polarization effects. As the temperature rises beyond this transition, ε′ becomes negative, indicating a change in the dielectric response. This negative permittivity results from displacement currents associated with thermally activated free carriers oscillating out of phase with the applied electric field, consistent with Drude-type conduction.

A similar frequency-dependent permittivity curve is observed in the SGR2 composite (Figure. 7.3), indicating that the behavior cannot be explained solely by free-carrier plasma oscillations. This suggests that bound charge oscillations coexist with the free-carrier response, implying contributions from both localized and itinerant charge carriers. Therefore, a more comprehensive model is required to accurately describe the frequency-dependent permittivity of these graphene/$SnO_2$ composites

While exact thresholds are limited by data resolution, combined analysis and previous work on SMS materials suggest that the conductivity required for negative permittivity falls between 0.1 and 0.5 S/m. In this study, the SGR2 composites help narrow this range further, indicating a more precise minimum threshold conductivity. According to this, around 0.2 S/m will be required and sufficient to achieve epsilon-near-zero behavior, and above 0.5 S/m, the material exhibits strongly negative permittivity. **This relationship is visualized in Figure 7.5**, which illustrates the transition from near-zero to negative permittivity as a function of conductivity for both SMS and SGR systems, offering a clearer understanding of the critical thresholds.

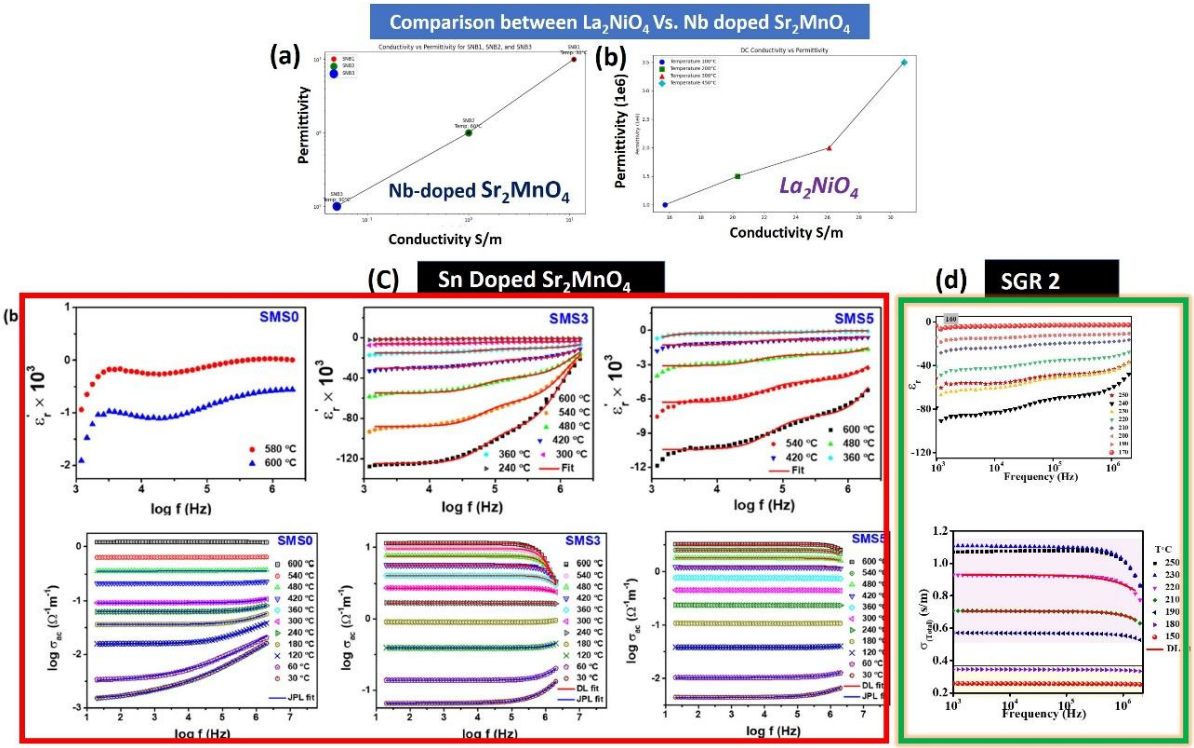


***Figure 7.5 (a) and (b) present a comparative analysis of $La_2NiO_4$ and Nb-doped $Sr_2MnO_4$, highlighting the correlation between electrical conductivity and permittivity. Both materials exhibit a consistent trend where increased conductivity is accompanied by corresponding changes in permittivity. Figure (c) shows the frequency-dependent permittivity and conductivity behavior of the SMS system (Red boxed), which closely resembles that observed in SGR2 (Green boxed) as seen in (d). This similarity confirms the presence of a bound charge relaxation process, characteristic of Drude-Lorentz-type dielectric behaviour.***

Upon further increasing the graphene content to 4 wt.% (SGR4), the composite exhibits a transition to a highly conductive regime, with the real part of permittivity (ε′) becoming strongly negative at room temperature. The magnitude of ε′ exceeds the upper detection limit of the LCR meter (ε′ ~ $10^{10}$), indicating a dominant free-carrier response. This is consistent with the emergence of an extended percolative network that enables continuous carrier transport throughout the matrix.

Conductivity measurements confirm a significant increase in DC conductivity, reaching ~6400 S/m—comparable to values observed in poor metals or heavily doped semiconductors. The abrupt rise in conductivity, relative to the sub-threshold sample (SGR2), signifies that the system has crossed the percolation threshold and entered a metallic-like transport regime. As shown in Figure7.6 (a) and (b), the frequency-dependent conductivity and permittivity of SGR4 follow the characteristic behavior of Drude-type free-carrier dynamics. Standard drude model of permitivty have been applied here owing to the conducting nature of the SGR 4 composite with no additional relaxation process.

Drude proposed a model to explain the behavior of conductivity in metal[36,235]:

$$\sigma_{ac} = \sigma_{dc} \frac{\omega_\tau^2}{\omega^2 + \omega_\tau^2} \qquad (7.9)$$

We applied Eqn. (7.9) for conductivity to fit the experimental data, as shown in Figures 7.6 (a) and (b). The strong agreement between the experimental data (symbols) and theoretical predictions (solid lines) suggests that the observed permittivity and conductivity are attributed to the plasma oscillations of free (delocalized) electrons. Unlike SGR2, the permittivity response of SGR4 lacks any discernible relaxation features, indicating that interfacial or dipolar polarization—typically associated with bound charges—is effectively suppressed. This behavior confirms that the observed negative permittivity in SGR4 arises primarily from the collective oscillations of delocalized charge carriers.

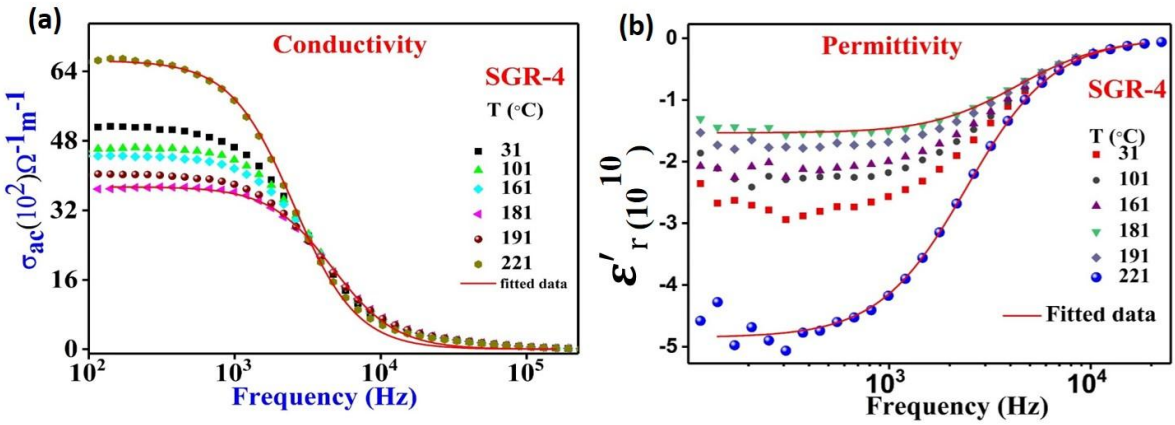


***Figure 7.6 (a) The total conductivity and corresponding (b) negative permittivity of SGR4***

## 7.6 Microstructure analysis and percolation mechanism:

To investigate the microstructural origin of the negative permittivity and to validate the proposed percolation mechanism, high-resolution field-emission scanning electron microscopy (FE-SEM) was performed on freshly fractured SGR pellets, as shown in Figure 7.7 (a–b). Prior to imaging, the pellets cleaned and polished using various grades of ambry paper, and then dried in a conventional oven at 100 °C to eliminate any residual moisture. The SEM images reveal a heterogeneous distribution of conductive and insulating phases, with localized regions of interconnected networks indicative of an evolving percolation pathway. This microstructural arrangement supports the transition to negative permittivity observed at elevated temperatures.

In SGR2, the graphene nanoplatelets are sparsely distributed, lacking continuous percolative pathways. However, efficient charge transport does not necessarily require geometrically continuous conduction paths; instead, electrical conduction can proceed via **quantum tunneling** across sub-nanometer gaps or **thermally activated hopping** over slightly larger distances[138]. These mechanisms are particularly relevant near the percolation threshold, where short-range electronic coupling between closely spaced conductive fillers can contribute significantly to the overall conductivity. In contrast, SGR4 exhibits a densely interconnected

microstructure, with graphene-rich domains forming quasi-continuous conductive clusters. The high surface-to-volume ratio and extensive interfacial contact of the nanoplatelets promote the formation of strong percolation networks, resulting in obvious increase in conductivity. This transition reflects a shift to network-mediated charge transport, distinct from intrinsic metallic conduction.

The experimental densities of the SGR pellets were measured using Archimedes' principle. Each measurement was performed three times, and the average value is reported. Since the pellets were not sintered at high temperature after compaction, their densification was limited, resulting in reduced compactness and hardness due to insufficient thermal energy for grain growth and pore elimination. The measured density of the SGR2 pellet containing 2% graphene was 5.8±0.4 g/cm$^3$, while that of the SGR4 pellet with 4% graphene was 5.5+0.9 g/cm$^3$

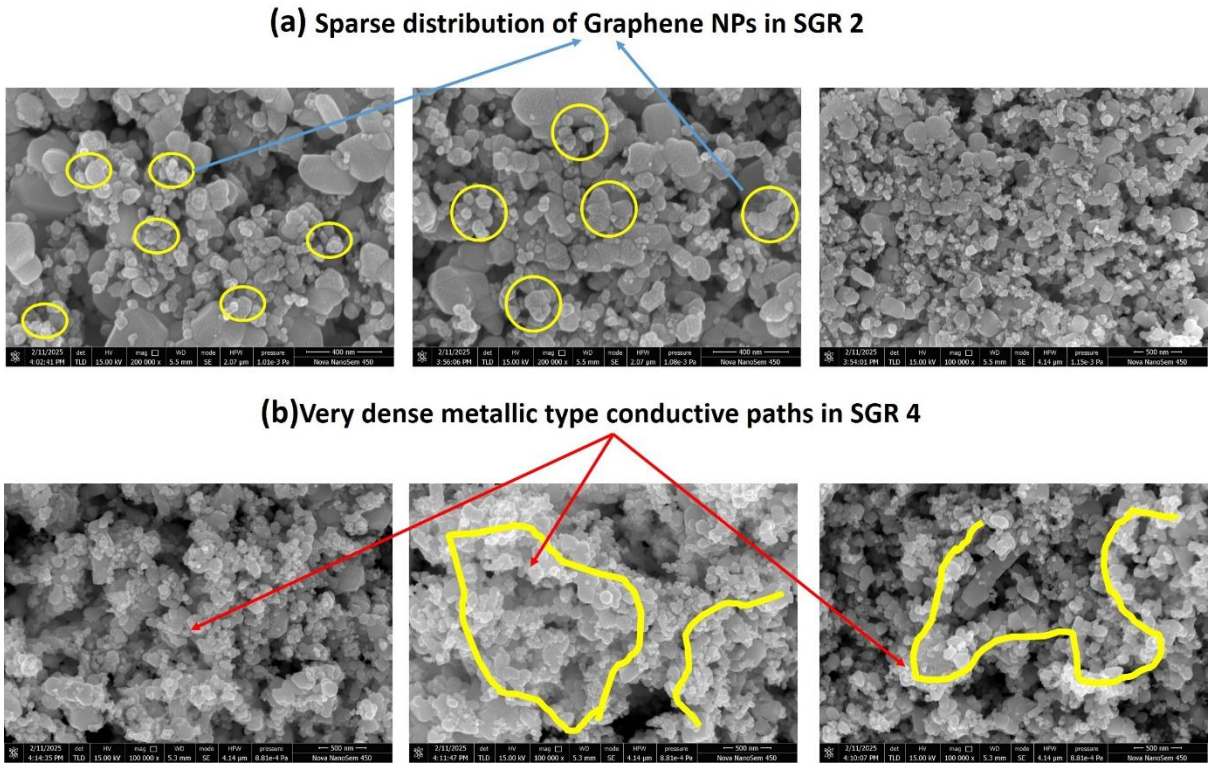


***Figure 7.7 Micrographs of SGR composites: (a) In SGR 2, sparsely distributed graphene nanoparticles lack continuous percolation paths, but close proximity may enable quantum tunneling at elevated temperatures, contributing to negative permittivity. (b) In SGR 4, nanosized graphene particles form metal-like closed loops, leading to enhanced electrical conductivity.***

## 7.7 EMI Shielding Effectiveness

To evaluate the electromagnetic interference (EMI) shielding performance of the prepared composites, SGR2 and SGR4, microwave frequency analysis was conducted in the X-band (8.2–12.4 GHz) using a vector network analyser. Scattering parameters ($S_{11}$ and$S_{21}$) were measured to analysis the reflection and transmission behaviour of the samples. A higher $S_{11}$ value indicates higher reflection of incident electromagnetic waves, while a lower $S_{21}$ corresponds to better attenuation of transmitted waves—both critical for effective EMI shielding. The total shielding effectiveness (SE) was calculated using standard formulations.

Total shielding effectiveness ($SE_T$) would be given by:

$$SET = SEA + SER \qquad (7.10)$$

$$SE_A = 10 \log \left(\frac{10^{\frac{S21}{10}}}{1 - 10^{\frac{S11}{10}}}\right) \qquad (7.11)$$

$$SE_R = 10 \log \left(1 - 10^{\frac{S11}{10}}\right) \qquad (7.12)$$

Where, $SE_A$ is shielding due to absorption, and $SE_R$ shielding due to reflection.

When an electromagnetic (EM) wave encounters the surface of a material, part of the wave is reflected, while the remainder is transmitted into the material. The relative proportions of reflection and transmission are governed by the degree of impedance mismatch between the material and free space[129,236].

$$Z = \sqrt{\frac{j\omega\mu}{\sigma + j\omega\varepsilon}} \qquad (7.13)$$

where:

- $\omega$ is the angular frequency of the incident wave,
- μ is the magnetic permeability,
- ε is the electric permittivity,
- σ is the electrical conductivity.

This equation shows how a material responds to electromagnetic waves, taking into account both how well it conducts electricity and how it stores electric energy. As the material becomes

more conductive, its impedance goes down, meaning it resists the wave less. As a result, more of the wave get reflected, making the material appear more reflective.

The key mechanism of electromagnetic shielding begins with **impedance mismatch**. When $Z \ll Z0$, a large discontinuity exists at the boundary. To satisfy Maxwell's boundary conditions (continuity of tangential E and H fields), the wave cannot fully enter the material and a **reflected wave** is generated. This reflection is quantified by the Fresnel reflection coefficient at normal incidence: For free space, the **characteristic impedance and reflection is** is given by

$$Z = \sqrt{(\mu_0 / \varepsilon_0)} \sim 377\ ohm \qquad (7.14)$$

$$R = \left|\frac{Z - Z_0}{Z + Z_0}\right|^2 \qquad (7.15)$$

In the limit$Z \ll Z0, R \to 1$, indicating strong reflection. Such behavior is characteristic of **good electromagnetic reflectors**, notably **metals** and **plasmas**, where high conductivity or negative permittivity (below plasma frequency) leads to low intrinsic impedance. Similarly, **epsilon-negative (ENG) materials**, where$Re[\varepsilon] < 0$, also exhibit low impedance and reflect incident EM waves efficiently due to their metallic-like response. On the other hand, when Z>Z0, the material allows **transmission** of EM waves in the materials. However, transmission alone does not imply effective **attenuation/absorption**.

For EM energy to consumed/ absorbed within the material, two conditions must be satisfied:

1. **Impedance matching**: Achieved when Z≈Z0, ensuring minimal reflection and maximal wave penetration into the material.

2. **Loss mechanisms**: The material must possess either finite conductivity (for ohmic loss) or structural features (e.g., porosity, graded refractive index) that increase energy dissipation through scattering, absorption, and heat conversion.

Where, $Z_0 \approx 377\ \Omega$ is the intrinsic impedance of free space, and $\varepsilon_r = \varepsilon / \varepsilon_0$. As $\varepsilon' \to 0$, the impedance $Z$ becomes large, and when accompanied by moderate dielectric loss ($\varepsilon'' > 0$), it approaches values that minimize reflection from free space.

The observed ENZ behavior in SGR2 indicates that the composite contains enough free carriers to facilitate interaction with incident electromagnetic waves. The dielectric response of $SnO_2$ controls the conductivity of graphene, leading to a tunable effective medium. This interplay regulates the real part of the permittivity toward zero while maintaining moderate loss ($\boldsymbol{\varepsilon''} = \boldsymbol{\sigma / \omega \varepsilon_0}$), bringing the system close to impedance matching with free space. As a result, reflection is suppressed and electromagnetic absorption is enhanced. This effectively dissipated as heat or bound charge oscillations. The power dissipated per unit volume under an oscillating field $E(t)$ is given by:

$$P_{loss} = \left(\frac{1}{2}\right) \omega\ \varepsilon_0 \varepsilon'' |E|^2 \qquad (7.16)$$

indicating that even small but finite $\varepsilon''$ can lead to substantial absorption if the field penetrates the material.

Figure 7.7 (a-b), presents the shielding effectiveness of SGR-2 along with the $\varepsilon''$ in Figure 7.7 (c), indicating a dominant contribution from absorption over reflection. This behavior is attributed to the epsilon-near-zero (ENZ) response and a high dielectric loss ($\varepsilon'' \sim 10^9$). The composite's porous microstructure further facilitates electromagnetic wave penetration, aiding

interaction with mobile charge carriers and subsequent dissipation via Joule heating. In contrast, the SGR-4 composite exhibits a highly reflective surface, with a maximum shielding effectiveness of 75 dB, attributed to its high electrical conductivity as shown in Figure 7.8 (d-e).

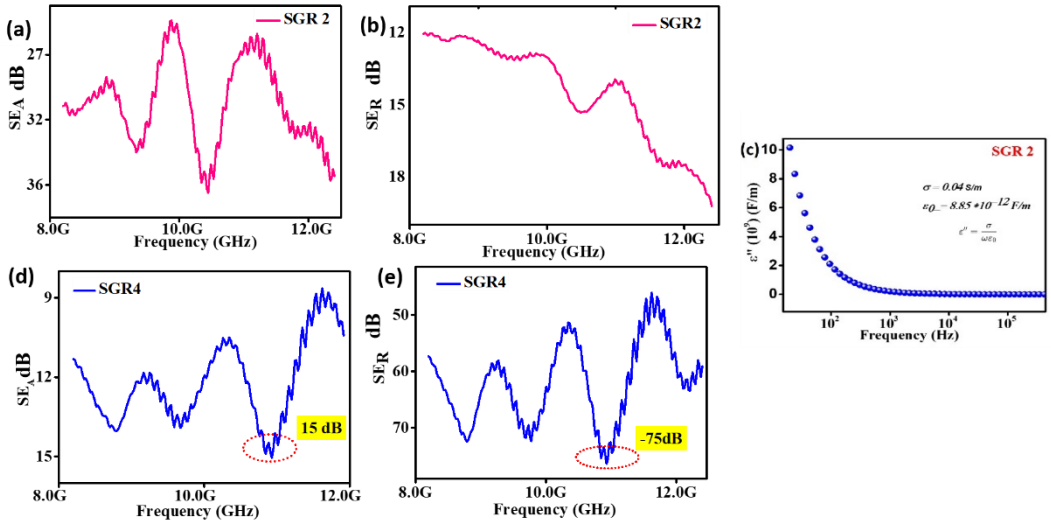


***Figure 7.8 The SE of the SGR composites (a) the effective shieling mechanism in SGR 2 is absorption however less reflection is measured in (b). (c) very high value of ε" is indicating the conduction loss in the materials. (d-e) In SGR4 very less absorption but large reflection, value is measured due to very high conductivity.***

## 7.8 Conclusion

This study highlights the strategic design of multifunctional and tunable material systems for better electromagnetic shielding with minimum transmission. We investigated two fundamentally different types of negative permittivity systems (Drude and Drude Lorentz), providing insights into their physical origins and mechanisms. A key outcome of this work is the experimental identification of a threshold electrical conductivity necessary for the existence of negative permittivity at room temperature—an important benchmark for practical applications. Additionally, we introduced a new class of negative permittivity materials, known as epsilon-near-zero (ENZ) materials. Microwave characterization and their shielding

effectiveness studies demonstrated that ENZ materials exhibit higher absorption capabilities, whereas materials with more negative permittivity tend to be highly reflective. These results underline the distinct roles of material conductivity and dielectric response in determining electromagnetic shielding behavior and pave the way for advanced applications in tunable metamaterials, sensors, and stealth technologies that too in cost effective way.